Int J Adv Manuf Technol (2012) 60:995–1007
DOI 10.1007/s00170-011-3655-1

ORIGINAL ARTICLE

Finite element analysis of laser inert gas cutting on Inconel 718

K. Y. Nyon · C. Y. Nyeoh · Mohzani Mokhtar · Razi Abdul-Rahman

Received: 30 November 2010 / Accepted: 19 September 2011 / Published online: 13 October 2011

Abstract Inconel 718 has high strength, which makes it difficult to cut using conventional cutting methods. In the present study, the laser inert gas cutting of Inconel 718 was simulated by finite element analysis software ANSYS. Finite element method was used to predict thermal stress and kerf width formation during the laser cutting process. ANSYS Parameter Design Language was used to model the Gaussian-distributed heat flux from the laser beam acting on the workpiece. The removal of melted material during laser cutting to form the kerf width was modeled by employing the element death methodology in ANSYS. In addition, laser cutting was simulated at continuous wave (CW) and the effects of laser power and cutting speed on kerf width were investigated. A series of experiments were carried out to verify the predictions. The temperature fields on the workpiece were measured using thermocouples. The kerf width size was measured using a profile projector, whereas the metallurgical and morphological changes at the cutting edge were examined using scanning electron microscopy. A good correlation was found between the simulation and experimental results.

Keywords Inconel 718 · Laser inert gas cutting · Finite element analysis · Thermal stress · Kerf width

K. Y. Nyon (✉) · C. Y. Nyeoh · M. Mokhtar · R. Abdul-Rahman
School of Mechanical Engineering,
Universiti Sains Malaysia (USM),
14300 Nibong Tebal, Penang, Malaysia
e-mail: nkeny84@yahoo.com

C. Y. Nyeoh
Faculty of Engineering & Technology,
Multimedia University (MMU),
75450 Jln Ayer Keroh Lama, Melaka, Malaysia

1 Introduction

Laser cutting is a non-contact thermal cutting process that uses laser to cut the workpiece into the desired geometry. A fully penetrated narrow cut kerf is generated by moving a focused laser beam along the surface of the workpiece. The most significant feature of laser cutting is its capability to generate a highly concentrated heat power to perform fast processing with high precision, resulting in high-quality product. These characteristics make laser suitable for cutting Inconel 718, intricate material to process due to its high strength and quality, for application in the aerospace and automotive industries. However, the high-temperature gradient in the cutting edge results in excessive thermal stress developed in this region and reduces quality [1]. This characteristic is particularly important in high-end applications. In cutting nickel-based alloys such as Inconel 718, high-pressure gas nitrogen is mostly used as an inert gas to produce burr and oxide-free cuts. Nitrogen as an inert gas is also used to eject the molten material without causing chemical reaction unlike the use of oxygen as inert gas [2]. Therefore, the kerf width is possible to predict a sufficiently strong nitrogen jet to blow the molten material out of the cut kerf. Laser cutting generally involves a number of variables: laser beam power, cutting speed, type of assist gas, and assist gas pressure. Each of these parameters must be fully specified and optimized. The model in the current study utilizes the finite element simulation technique to predict the thermal stress and kerf width developed during laser cutting. Therefore, the experimental cost is reduced.

Numerous research studies have been carried out to analyze the heat transfer during laser material processing. A mathematical model was developed by Joseph et al. [3] to estimate the heat conduction losses during laser cutting. They predicted the cutting speed and the temperature field

in the heat-affected zone (HAZ). The temperature field during laser forming of sheet metal was modeled by Ji and Wu [4]. The simulation results showed an increase in the peak values of temperature with an increase in laser output power. However, temperature was found to decrease with an increase in cutting speed and workpiece thickness. The temperature trends in cutting ceramics preheated by carbon dioxide (CO_2) laser were also analytically investigated by Ho et al. [5]. They observed that the laser power level and cutting speed rate have significant effects on temperature.

A number of researches have also been conducted in the area of finite element-based numerical simulation techniques to examine laser material processing. A numerical model was developed by Paul and Vinay [6] to estimate HAZ formation in the laser cutting of stainless steel. Their method identified the optimum process parameters for laser cutting. The evaporative laser cutting process was modeled by Meung [7]. He evaluated the groove shapes and temperature distributions during the laser cutting process. Thermal stress developed during the laser cutting of ceramic was studied by Akarapu et al. [8]. In their model, a probabilistic fracture model was introduced to assess the failure possibility during laser cutting and forming processes. Laser marking on an eggshell was conducted by Chen et al. [9]. They established the temperature model of the eggshell and predicted the heat-affected area by applying a Gaussian-distributed laser beam acted on the surface. The finite element model on the laser removal of titanium nitride from coated carbide substrate was developed by Sundar et al. [10]. In this model, the ablation of the material was simulated by the removal of the elements with a temperature higher than the melting temperature of the material.

Comparatively, few research studies have been conducted on the thermal stress of laser cutting at different shapes and thicknesses of metals [1, 11–15]. Previous research introduced a constant temperature heat source at the melting temperature of the material for the laser beam in the finite element simulation. In this study, a Gaussian-distributed heat source is adopted as the laser heat source in modeling laser cutting. The temperature and stress fields of the workpiece are computed using finite element method (FEM). This model is also capable of predicting kerf width formation on laser inert gas cutting. The laser cutting experiment was performed with the same cutting parameters used in the simulation. Thermocouples were used to measure the temperature of the workpiece, whereas the kerf width size was measured using a profile projector and compared with the simulation prediction. Meanwhile, a scanning electron microscope (SEM) was used to inspect the metallurgical and morphological changes in the cutting edge. Inconel 718 sheets with the thicknesses of 1 and 2 mm were used in this study. The simulations and experiment were done with five levels of laser cutting powers and cutting speeds.

2 Experimental

Experimental verification was performed to validate the simulation model. Figure 1 shows a schematic illustration of the laser cutting system and the temperature measurement devices. The principal components are the laser, laser beam, mirrors, focusing lens, gas nozzle, cutting gas, and the workpiece. The laser beam passes through a mirror and a guide mirror before reaching the focusing lens. At a suitable standoff distance, the laser beam is focused on the workpiece and performs the cutting operation. The cutting gas assists the cutting by removing the molten metal from the workpiece.

Trumatic L3030 CO_2 laser cutting machine with a maximum power output of 2,700 watts was used in the laser cutting experiment. A focal lens of 127 mm was used to focus the laser beam to a diameter of 0.3428 mm. Nitrogen emerging from a conical nozzle was used as an assist gas. In the experiment, 50-mm straight cuts were performed on Inconel 718 with the thicknesses of 1 and 2 mm. For each thickness, two experiments were carried out. The objective of the first experiment is to study the effect of laser power on the kerf width changes while the value of cutting speed is fixed to a minimum. Meanwhile, in the second experiment, the value of laser power was set to a maximum in order to study the effect of the cutting speed on the kerf width changes. The laser cutting parameters are presented in Table 1. A total of three exposed junction thermocouples (type K) connected to a data logger system were used to record the temperature history on the workpiece. The thermocouples named as TC1, TC2, and TC3 were placed at the different locations as shown in Fig. 2. On the top surface, thermocouple TC1 is installed at a distance of 8 mm from the generated cutting line to avoid collision between the cutting head and the thermocouple. While on the bottom surface, thermocouple TC2 is installed at 2 mm and TC3 is installed at 8 mm from the generated cutting line. The temperatures at the top and bottom surfaces were compared using TC1 and TC3.

A profile projector was used to measure the keft width of the workpieces, and a SEM was employed to capture the micrographs of the cutting edge after the laser cutting process.

3 Theory and simulation

As mentioned earlier, laser cutting is a thermal cutting process. The laser beam is focused on the workpiece which is heated locally. Some of the laser energy is absorbed by the material while the rest is reflected. The absorbed laser energy is then conducted into the material and is lost as heat through convection from the surface. The efficiency of laser

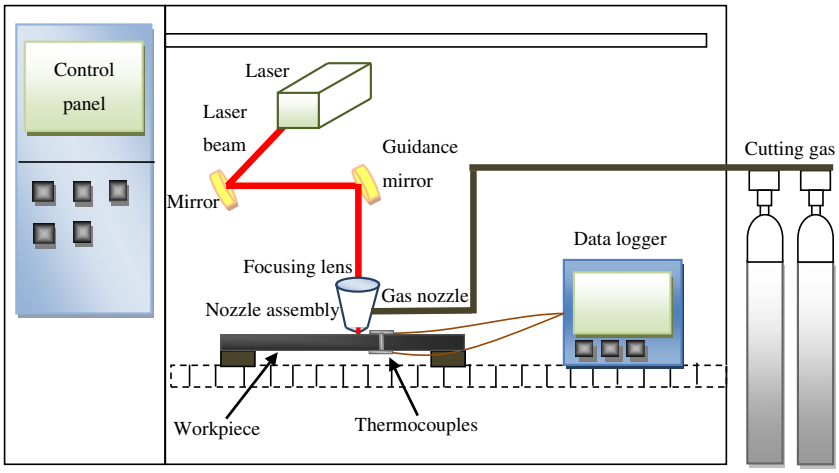

Fig. 1 Schematic diagram illustrating the experimental set up of laser cutting system and temperature measurement devices

energy absorbed by the material depends on the thermal and optical properties of the material as well as, the wavelength of the laser beam, its polarization, and the temperature of the workpiece [7]. The molten material is blown out, and a kerf develops due to the assist gas pressure flow.

The parameters controlling the laser cutting operation are the laser power, cutting speed, assist gas pressure, material thickness, material reflectivity, thermo-physical properties, and the beam diameter. All of these parameters have an effect towards the cut quality and performance of the cutting operation.

Table 1 Laser cutting parameters used in the study

Workpiece thickness		Cutting speed (mm/min)	Laser power (W)
1 mm	Experiment 1	4,080	800
			1,000
			1,200
			1,400
			1,600
	Experiment 2	4,080	1,600
		5,100	
		6,120	
		7,140	
		8,160	
2 mm	Experiment 1	4,080	1,600
			1,800
			2,000
			2,200
			2,400
	Experiment 2	4,080	2,400
		4,620	
		5,160	
		5,700	
		6,240	

Therefore, the following assumptions are made in deriving the model in ANSYS:

1. The material is isotropic and opaque.
2. The spatial distribution of the laser beam is in Gaussian at TEM_{00} mode.
3. With an appropriate depth of focus, the laser energy density is equal along the thickness of the workpiece.
4. The molten material is removed immediately from the workpiece by an assist gas pressure. Thus, no vaporization occurs.
5. Phase change is neglected due to small fraction of the re-solidified region.
6. The cooling effect of the inert gas is negligible.

3.1 Laser heat source modeling

Heat source modeling is the most important part in the thermal analysis of laser cutting. Various beam shapes including Gaussian, circular, rectangular, etc., can be obtained by using the beam-shaping method for different kinds of applications in laser material processing. Among these, the Gaussian energy distribution is the most preferred mode for laser cutting because a very small diameter can be focused, resulting in a higher power density [16]. The laser

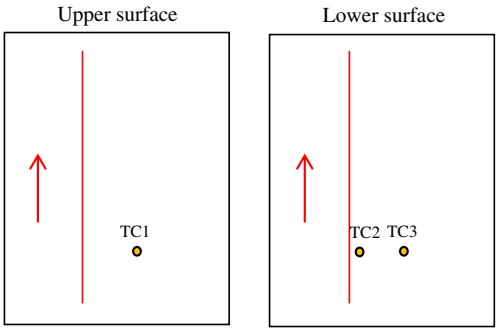

Fig. 2 Locations of the thermocouples at the top and bottom surfaces

energy that is transmitted to the target material at a depth, z, is governed by the Beer–Lambert law given by:

$$S_o(z) = I_o e^{-\delta z} \quad (1)$$

where:

P Laser beam power output (W)
I_o $P/\pi r^2$, laser intensity at (0, 0) (W m^{-2})
δ Absorption coefficient (m^{-1})

However, for metals, the absorption coefficient is around 5×10^7 m^{-1}. Therefore, the absorption of laser energy takes place in a very shallow region with a depth of only a fraction of the wavelength of the incident radiation [17]. Surface heat flux (W m^{-2}) is adequate in presenting the heat source from the laser beam in the calculation expressed follows:

$$S_o(x,y) = I_o(1-R)e^{\left(-\left(x^2+y^2\right)/r^2\right)} \quad (2)$$

where:

r Radius of the beam (m)
R Surface reflectivity
x, y Distance from center (0, 0) of the laser beam in x- and y-direction (m)

Equation 2 is used for CW cutting condition. The Gaussian beam profile as shown in Fig. 3 is used as the heat source at TEM_{00} mode. The absorptivity of Inconel 718 at 10.6 μm (CO_2) wavelength determined by Sainte-Catherine et al. [18] is used in the calculation.

3.2 Heat transfer analysis

Heat transfer in the laser cutting process is modeled as transient and three dimensional (3D). The general mathematical model for transient temperature is written as:

$$\rho c(T)\frac{\partial T}{\partial t} = \frac{\partial}{\partial x}\left(k(T)\frac{\partial T}{\partial x}\right) + \frac{\partial}{\partial y}\left(k(T)\frac{\partial T}{\partial y}\right) + \frac{\partial}{\partial z}\left(k(T)\frac{\partial T}{\partial z}\right) + Q_{\text{int}} \quad (3)$$

where:

ρ Material density (kg m^{-3})
$c(T)$ Specific heat as a function of temperature (J kg^{-1} K^{-1})
$k(T)$ Thermal conductivity as a function of temperature (W m^{-1} K^{-1})
Q_{int} Internal heat generation rate (W m^{-3})

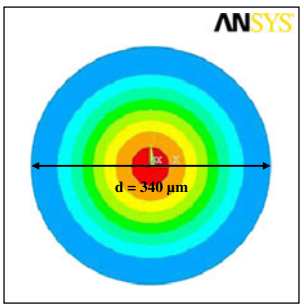

Fig. 3 Gaussian-distributed heat flux of a laser beam

To solve the above differential equation, the boundary and initial conditions must be identified. Free convection to the atmosphere is assumed to be present on the surfaces of the workpiece. The general boundary condition is presented in the following Eq. 4 below:

$$q_{\text{freeconv}} = h_{\text{freeconv}}(T_s - T_{\text{amb}}) \quad (4)$$

where:

T_s Surface temperature of the workpiece
T_{amb} Ambient temperature (307 K)
h_{freeconv} Convective heat transfer coefficient of air (15 W K^{-1} m^{-2})

Initially, the workpiece is assumed to be at constant ambient temperature, i.e., $T = T_{\text{amb}}$. The temperature-dependent thermal properties of Inconel 718 used in the calculation are shown in Table 2. Equation 3 is solved numerically with the appropriate boundary conditions to predict the temperature field in the workpiece.

3.3 Material removal

The laser energy absorbed by the workpiece caused the temperature values to reach the melting point due to the laser focused radiation. The molten material is ejected immediately by an assist gas pressure and forms the kerf avoids a further increase in temperature to the boiling point or beyond. Subsequently, a small fraction of a liquid layer re-solidifies at the cutting edge.

The melting speed or penetration speed can be calculated based on the energy balance of the material removed. Heat flow is assumed to be one dimensional and is used in the melting process (the heat conduction is zero). This fairly gross assumption is rational if the

Table 2 Thermal properties of Inconel 718 used in the simulation [24]

Temperature (K)	Thermal conductivity (W m^{-1} K^{-1})	Specific heat (J kg^{-1} K^{-1})	Melting range (K)
273	11	425	1,533–1,609
473	14	468	
673	18	511	
873	20	561	
1,073	23	594	
1,273	26	644	
1,473	29	683	
1,673	32	728	
1,873	35	772	

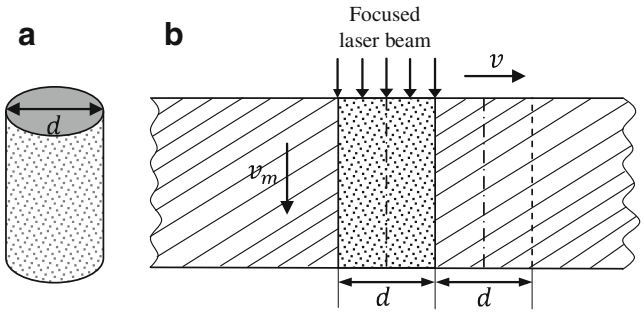

Fig. 4 **a** Cylinder with diameter, *d*. **b** Model to determine cutting speed, *v* (modified from Ref. [19])

melting speed is similar to or faster than the rate of conduction [2].

The energy required to melt a mass, *m* of a material in a cubic element (see Fig. 4) at an initial temperature (ambient temperature) is written as [19]:

$$E_m = \frac{\pi d^2}{4}\rho v_m t\left[C_s(T_m - T_{amb}) + L_f\right] \quad (5)$$

where:

E_m Energy required to melt the material (J)

Table 3 Mechanical properties of Inconel 718 used in the simulation [23]

Temperature (K)	Young's modulus (E (GPa))	Poisson's ratio (ν)	Thermal expansion coefficient ($\alpha \times 10^{-6}$ (K^{-1}))	Density (ρ (kg m^{-3}))
294	199.95	0.294	–	8,200
311	198.56	0.291	–	
366	195.81	0.288	13.2	
422	193.05	0.280	–	
478	190.29	0.280	13.6	
533	186.85	0.275	–	
589	184.09	0.272	13.9	
644	180.64	0.273	–	
700	177.88	0.271	14.3	
755	174.44	0.272	–	
811	170.99	0.271	14.6	
866	166.85	0.276	–	
922	163.41	0.283	15.1	
978	158.58	0.292	–	
1,033	153.75	0.306	16.0	
1,089	146.86	0.321	–	
1,144	139.27	0.331	–	
1,200	129.62	0.334	–	
1,255	119.97	0.341	–	
1,311	109.63	0.366	–	
1,366	98.60	0.402	–	

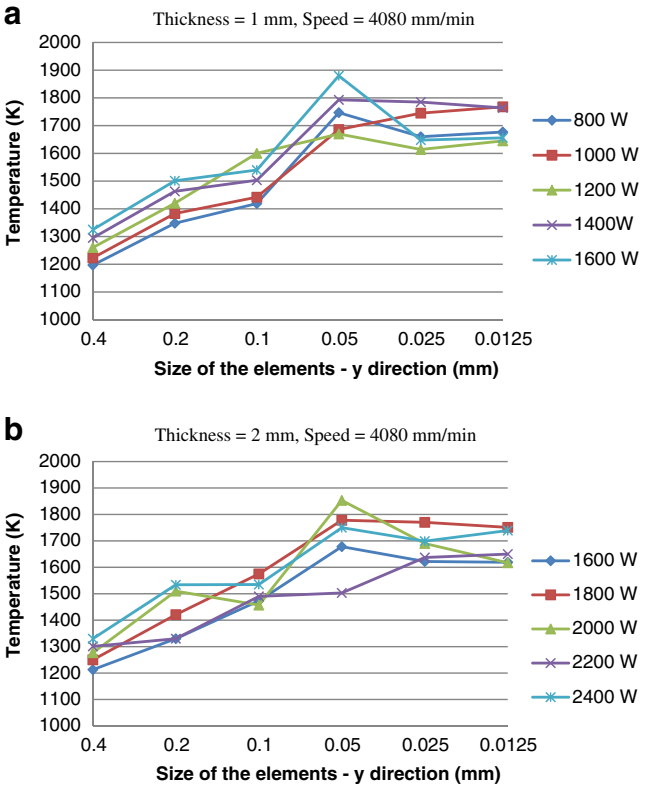

Fig. 5 Temperature plot for the mesh convergence parametric study of different laser powers for two thicknesses of Inconel 718: **a** 1 and **b** 2 mm

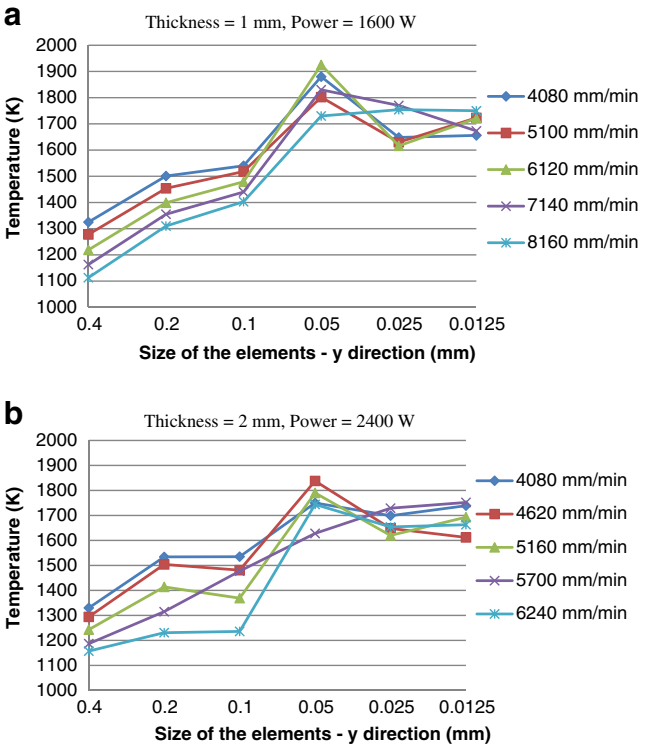

Fig. 6 Temperature plot for the mesh convergence parametric study of different cutting speeds for two thicknesses of Inconel 718: **a** 1 and **b** 2 mm

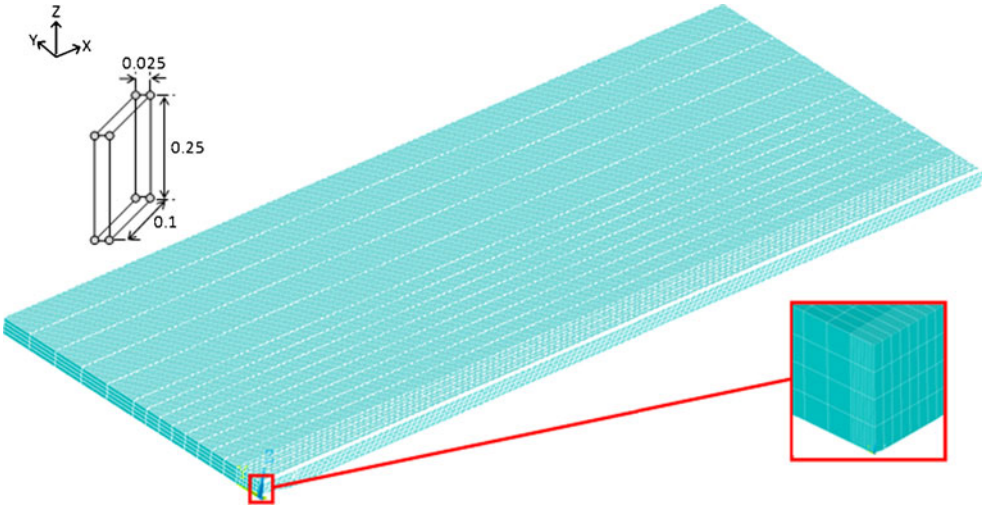

Fig. 7 Details of the mesh and the dimensions (unit in millimeters) of the elements at the boundary of the laser heat flux (1-mm-thick workpiece)

d	Laser spot diameter (m)	t	Time (s)
ρ	Mass density (kg m^{-3})	C_s	Specific heat capacity of solid (J kg^{-1} K^{-1})
v_m	Melting speed (m s^{-1})		

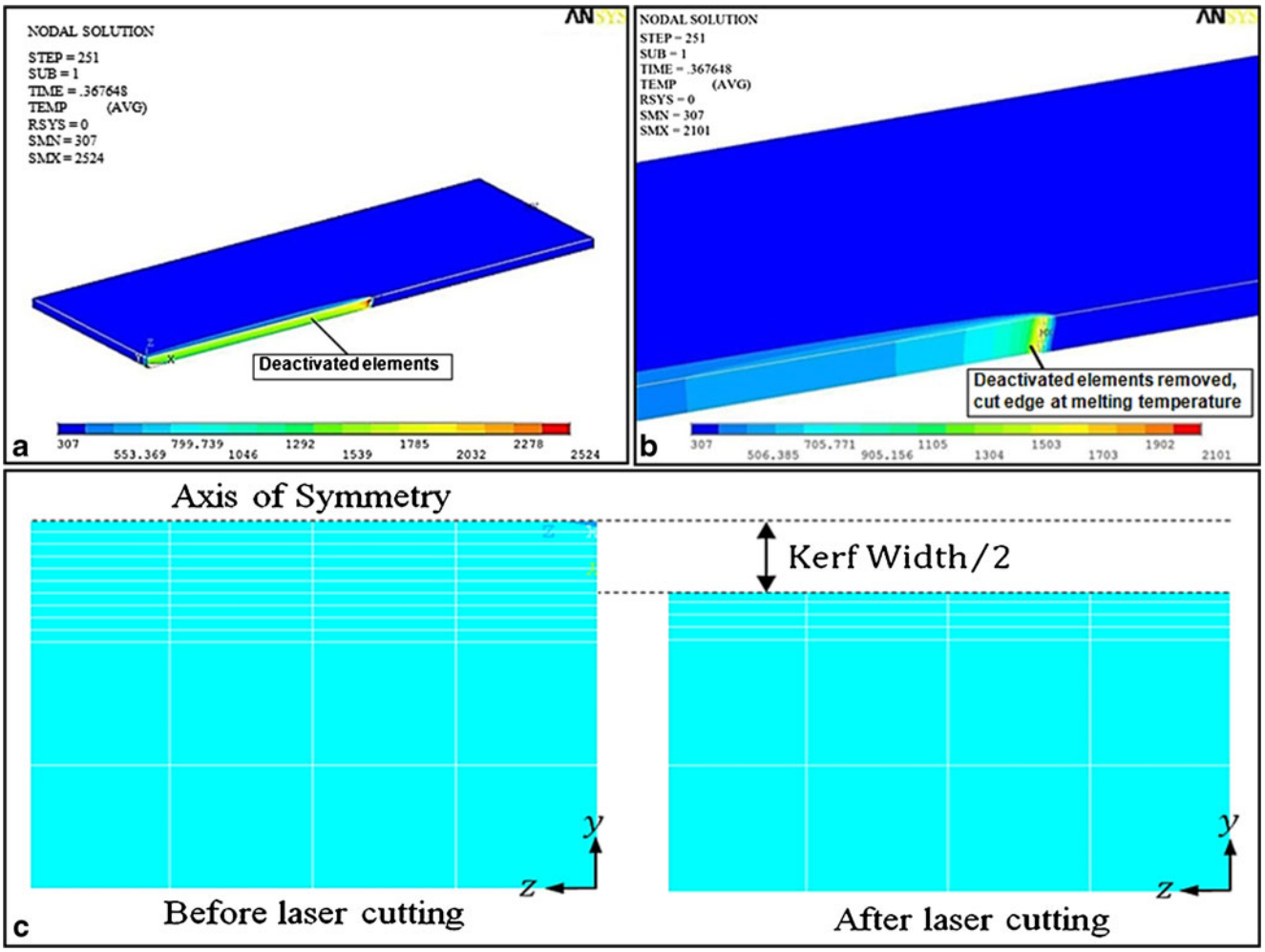

Fig. 8 **a** Deactivated elements. **b** Removal of deactivated elements and the cutting edge at the melting temperature of the material. **c** Kerf width calculation

T_m Melting temperature (K)
T_{amb} Ambient temperature (K)
L_f Latent heat of fusion (J kg^{-1})

In addition, the power required to melt the material is given by:

$$P_m = (1 - R)P = \frac{E_m}{t} \tag{6}$$

Therefore, the volume removed per second per unit area (melting speed) is determined by:

$$v_m = \frac{4(1 - R)P}{\pi d^2 \rho \left[C_s(T_m - T_{amb}) + L_f\right]} \tag{7}$$

3.4 Thermal stress analysis

As the laser spot moves, the heated zone cools down due to radial heat conduction and convection from the surfaces. Thermal stress develops from the rapid cooling rate of high temperature. The thermal stress caused by the temperature difference ΔT is written as:

$$\sigma_{them} = \frac{E\alpha\Delta T}{1 - \nu} \tag{8}$$

where:

E Young's modulus
α Thermal expansion coefficient
ν Poisson's ratio

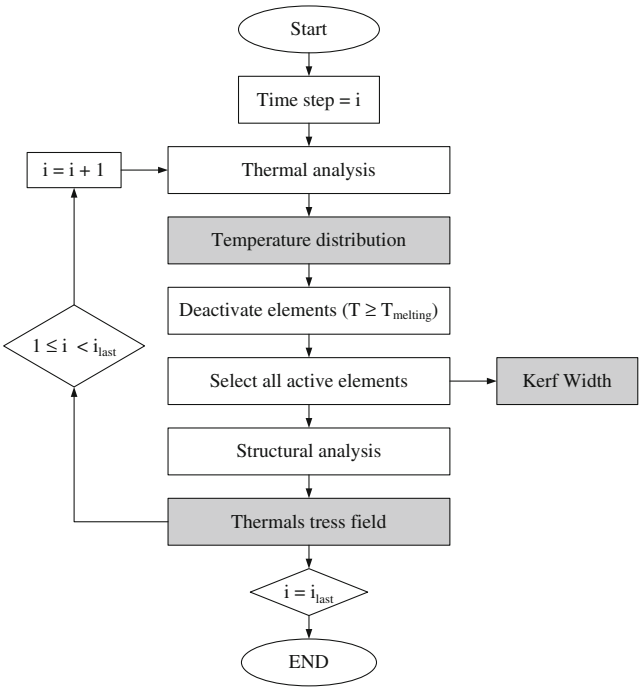

Fig. 9 Flow chart of the finite element simulation

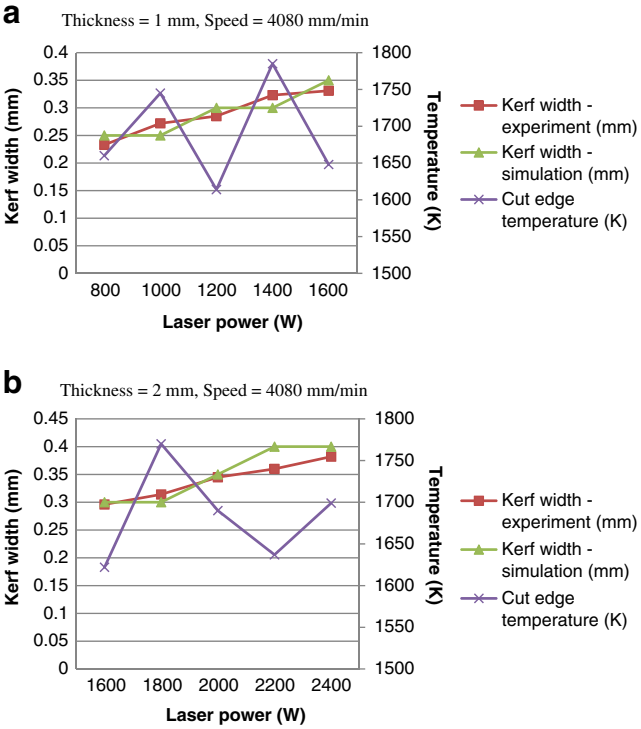

Fig. 10 Kerf width at different laser powers and temperatures of the cutting edge for two thicknesses of Inconel 718: **a** 1 and **b** 2 mm

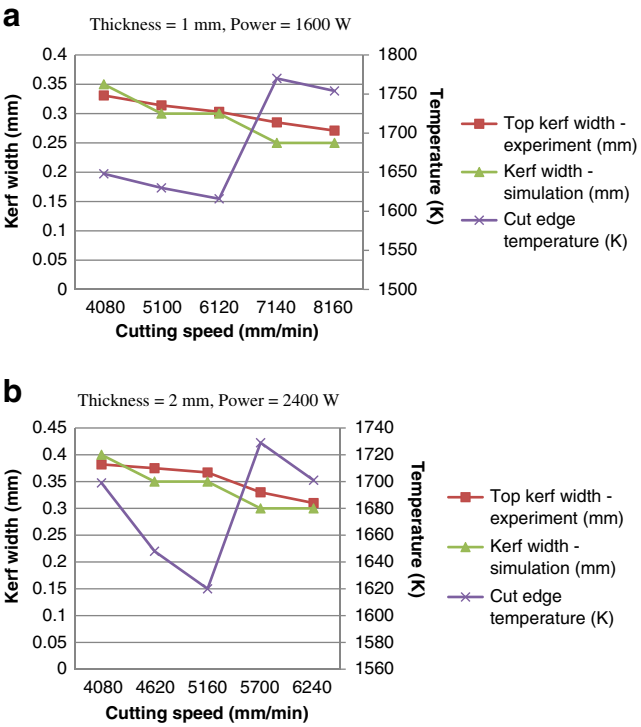

Fig. 11 Kerf width at different cutting speeds and the temperatures of the cutting edge for two thicknesses of Inconel 718: **a** 1 and **b** 2 mm

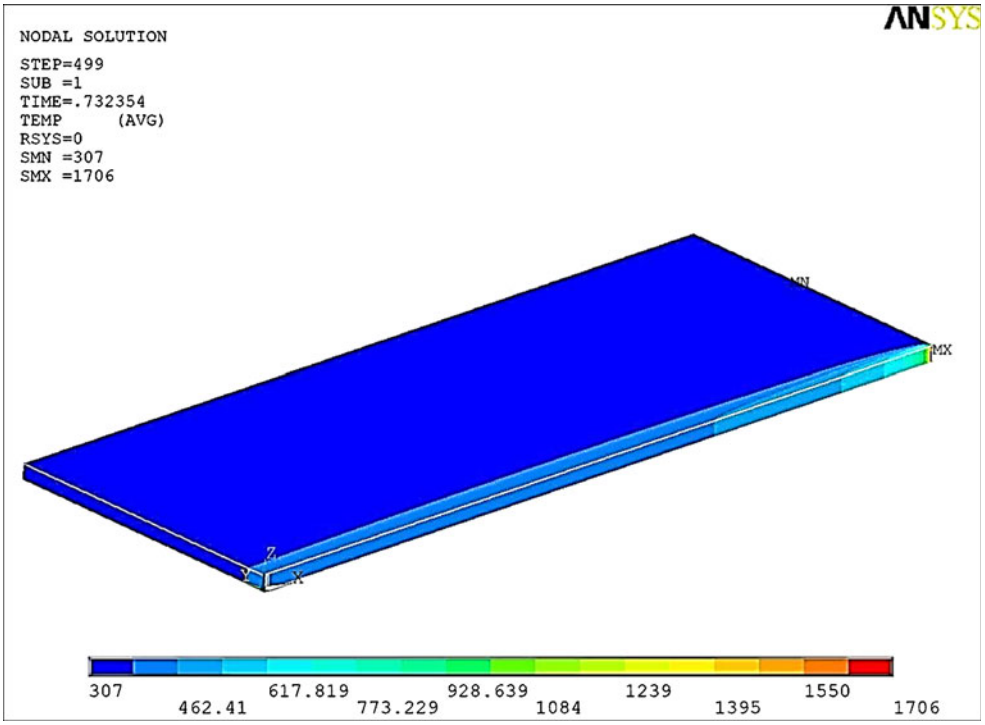

Fig. 12 3D view of the temperature distribution after the cutting process is complete for the workpiece with 1-mm thickness, 1,200 W laser power, and 4,080 mm/min cutting speed

The equivalent von Mises stress is given by the following expression:

$$\sigma_m = \sqrt{\frac{(\sigma_1 - \sigma_2)^2 + (\sigma_2 - \sigma_3)^2 + (\sigma_1 - \sigma_3)^2}{2}} \quad (9)$$

where σ_1, σ_2, σ_3 are the three principal stresses from any point in the x, y, or z directions of the principal axis obtained from Eq. 8. Plastic deformation occurs when σ_m reaches the yield strength of the material. The temperature-dependent mechanical properties of Inconel 718 used in the calculation are shown in Table 3. No external loads acting on the workpiece are assumed. The workpiece is clamped on one side, parallel to the cutting line.

3.5 Finite element simulation

Finite element simulations were performed using the same cutting parameters adopted in the experiment as shown in Table 3. The laser beam travels along the x-axis, (i.e., the symmetrical axis of the workpiece) (Fig. 7), only half of the workpiece is modeled to reduce the computational time. The effect of mechanical deformation on heat flow during laser cutting is found to be insignificant [13]. Therefore, a sequentially coupled physics analysis using FEM software ANSYS is performed to determine the temperature distribution and the resulting thermal stress in the workpiece. The results of the thermal analysis are treated as input for the structural analysis using ANSYS Parameter Design

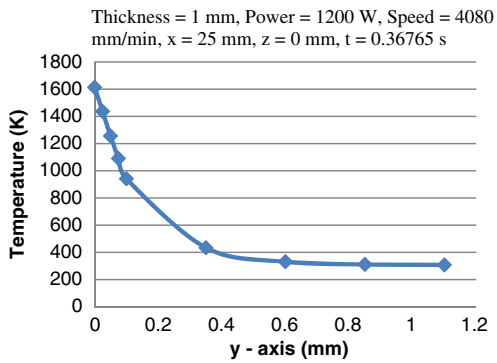

Fig. 13 Temperature distribution along the y-axis in the middle of the workpiece

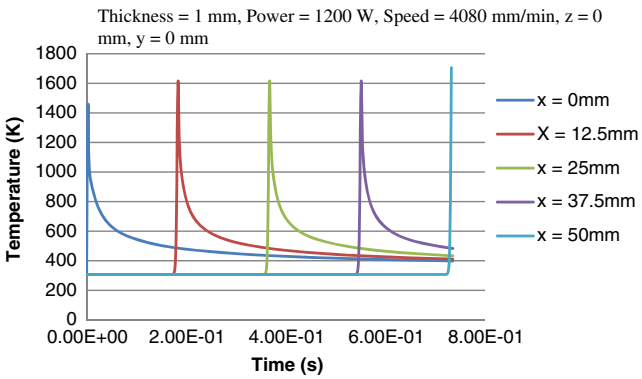

Fig. 14 Temporal variation in temperature at different locations of the cutting edge

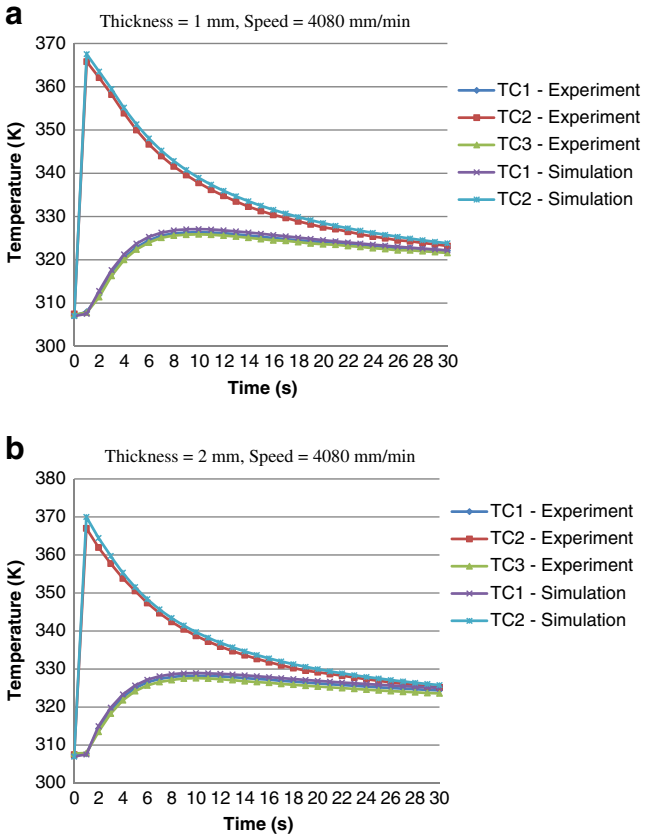

Fig. 15 Time–temperature curves: and comparison between the experimental and simulation results for two thicknesses of Inconel 718: **a** 1 and **b** 2 mm

Language (APDL) programming language. Both analyses are performed with the same mesh but different element types. Thermal element SOLID70 is used in the transient thermal analysis, whereas an equivalent structural element SOLID45 is adopted in the structural analysis. A detailed description of the elements can be found in [20].

Grid density is very important in finite element analysis because the coarseness of the grid can result in large errors. However, if the grid is too fine, the computational time increases. To determine an acceptable compromise between accuracy and computational time, mesh convergence parametric studies were conducted to obtain the appropriate element sizes, which are presented in Figs. 5 and 6. The figures clearly show that the size of the element at 0.025 mm is sufficient to achieve reasonable accuracy at different cutting parameters for both thicknesses. Hence, to optimize and balance the simulation accuracy and computational efficiency, 0.025 mm is selected as the size of the element in the y-direction at the boundary of laser heat flux. Further, variable meshes, with a very dense mesh at the boundary of the laser heat flux and a coarser mesh expanding gradually away from the cut edge were designed. A short cut of 50 mm was found to be adequate in the present study [1]. Therefore, with the workpiece dimension of 50×20 mm, the mesh comprises about 60,000 and 120,000 elements for the thicknesses of 1 and 2 mm, respectively. The details about the mesh are presented in Fig. 7.

Element death methodology was applied in the simulation by deactivating the elements when the element temperature, T is higher than the melting temperature, T_{melting}. These elements are deactivated or considered to be dead, (i.e., with insignificant effect in the subsequent time steps by setting the conductance to approximately zero) [20]. With the element death methodology applied in the simulation, the temperature of the cutting edge should be close to the melting temperature (1,609 K) of the material for all cutting parameters. From Figs. 5 and 6, the temperatures of the cutting edge vary for different cutting parameters as an element can only be deactivated if the average temperature of the element achieves the melting temperature of the material. In sum, a higher power and lower cutting speed increase the workpiece temperature and cause more elements to be heated at a temperature higher than the melting temperature of the material. Therefore, more elements are deactivated by the element death methodology applied in the simulation.

The position of the heat flux vector produced by the laser beam varies with time. In this study, the Gaussian-distributed heat flux (Fig. 3) was modeled using ANSYS APDL programming language. The position of the laser spot at time, t is defined using a table. The laser heat flux moves in the x-direction with a cutting speed, v and simultaneously penetrates into the workpiece in the z-direction with a melting speed, v_m. The laser beam power and cutting speed can be easily manipulated in the program.

To model the removal of molten material, the element death methodology (available in ANSYS) was employed in the simulation. At each time step, the elements with a temperature higher than the melting temperature ($T \geq T_{\text{melting}}$) of the material were deactivated. The deactivated elements represent the material that has been removed by the inert gas and thus forms the cut kerf. By setting the conductivity to approximately zero, these elements are considered to be dead, with an insignificant effect in on the subsequent time steps (Fig. 8a) [20]. The maximum temperature of the cutting edge (remaining) is about the same as the melting temperature of the material. This forms the constant temperature heat source of the melting temperature of the material moving at the cut edge as shown in Fig. 8b. The kerf width size is calculated using Eq. 10 (Fig. 8c):

$$\text{Kerf width size} = 2(\text{original workpiece size} - \text{remaining workpiece size}) \quad (10)$$

At the boundary of the laser heat flux, the element size in the *y*-direction is 0.025 mm. Therefore, the estimated kerf width has an accuracy of ±0.05 mm. The kerf width size at the top and bottom surfaces are the same due to a similar laser energy density along the thickness direction.

An overview the finite element simulation is presented in the flow chart in Fig. 9.

4 Results and discussions

The laser inert gas cutting of Inconel 718 sheet with the thicknesses of 1 and 2 mm were considered in this work. ANSYS finite element simulation with element death methodology was used to predict the kerf width, temperature fields and thermal stress developed during

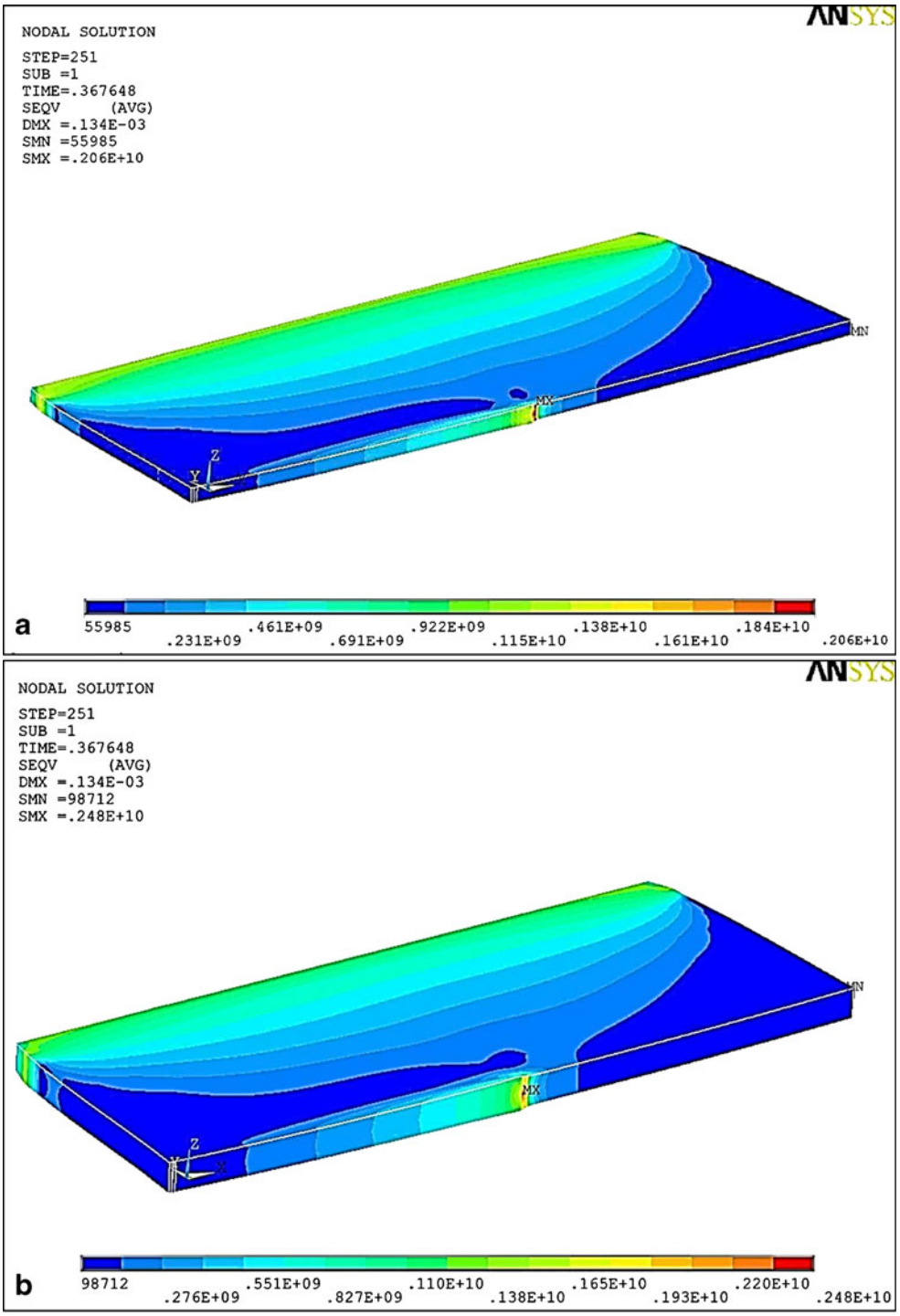

Fig. 16 3D view of the von Mises stress distribution for two thicknesses of Inconel 718: **a** 1 and **b** 2 mm

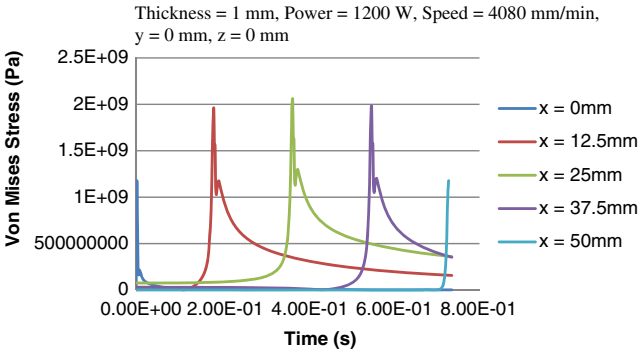

Fig. 17 Temporal variation in von Mises stress at different locations of the cutting edge

laser cutting. Experiments were conducted to verify the present predictions. In general, a higher laser power and lower cutting speed are required to perform a full penetration cut on the workpiece with a thickness of 2 mm compared with that which has a 1-mm thickness. A higher laser power is also required for high-speed cutting [2]. Therefore, to study the effect of laser powers on kerf width changes, the cutting speed is fixed at the minimum speed enough to produce a through cut. Meanwhile, laser power is fixed at its maximum in order to study the effect of cutting speeds on kerf width changes.

Figure 10 shows both the kerf width predicted from the finite element simulation and obtained from the experiment with different laser powers. The results of different cutting speeds are shown in Fig. 11. The predicted results showed good agreement with the experimental results. The predicted maximum temperature of the cutting edge is also presented in the figures. By increasing the laser power, the kerf width increases. By contrast, the kerf width decreases as the cutting speed increases. This trend is true for both workpiece thicknesses (1 and 2 mm). This is because higher power intensity increases the material removal rate from the kerf. In addition, increasing the laser cutting speed and maintaining the laser power reduce the material removal rate from the kerf [21]. From Figs. 10 and 11, the temperatures of the cutting edge are within the range of 1,614–1,785 K. This result is due to the element death methodology applied to deactivate the element when the temperature is higher than the melting temperature (1,609 K) of the material and when the element size is 0.025 mm. The material in this temperature range is in liquid form. This thin layer of liquid is re-solidified to form the recast layer, which shows good agreement with theory. For example, for laser power of 800 W, the predicted kerf width is 0.25 mm, and the temperature of the cutting edge is 1,660 K (Fig. 10a). As the laser power increases to 1,000 W, the predicted kerf width is maintained at 0.25 mm, the temperature of the cutting edge increases to 1,745 K. This result is due to the increase in the temperature of the elements as the laser power increases. However, this increase is not sufficient to cause more elements to be deactivated. For a laser power of 1,200 W, the predicted kerf width increases to 0.30 mm, and the temperature of the cut edge drops to 1,614 K as more elements are deactivated. This finding is true with an increase in cutting speed as shown in Fig. 11. Therefore, the predicted kerf width has an accuracy of ±0.05 mm.

For the workpiece with a thickness of 1 mm, the cutting parameters, such as a laser power of 1,200 W and cutting speed of 4,080 mm/min were selected for the further analysis of temperature and developed thermal stress. This choice is due to the close peak temperature of the cutting edge (1,614 K) to the melting temperature (1,609 K) of the material. The cutting edge temperature is controlled at 1,614 K for both thicknesses for comparison and the temperature profiles are also the same. Therefore, Figs. 12, 13, and 14 only show the thermal analysis results for 1-mm thickness. Fig. 12 also shows the 3D distribution of temperature after the cutting process was completed. The cutting edge temperature is the same as the melting temperature of the material, and it is decreased as it moves in the y-direction. The temperature along the y-axis is reflected in Fig. 13. The temporal variation in temperature at five locations of the cutting edge is shown in Fig. 14. At $x=0$, the temperature increased from 307 to 1,468 K. This increase comprises the initial transient stage. The peak temperature value, which remains constant at 1,614 K, is called the quasi-stationary stage. When the laser heat source reaches the end of the cutting process ($x=50$ mm), the peak temperature (1,706 K) becomes higher as the heat conduction is weak at the boundary of the workpiece.

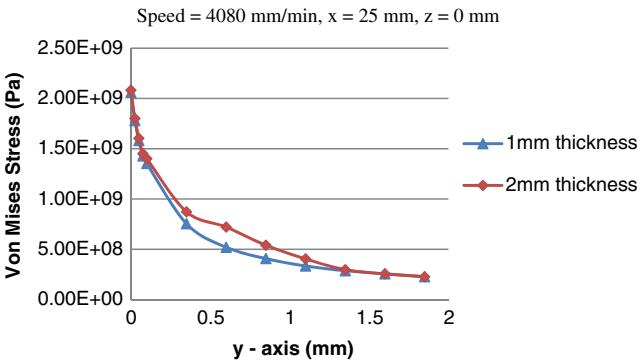

Fig. 18 Peak von Mises stress variation along the y-axis for two thicknesses

Table 4 Peak von Mises stress at the top, center, and bottom surfaces for two thicknesses (x=25 mm, y=0 mm)

Thickness (mm)	Peak von Mises stress (Pa)		
	Top (z=0 mm)	Center (z=thickness/2)	Bottom (z=thickness)
1	2.05E+09	2.06E+09	2.05E+09
2	2.08E+09	2.48E+09	2.08E+09

Figure 15 shows the comparison of temperature trends for the workpiece with 1- and 2-mm thicknesses. To verify the temperature measured by the thermocouples, the calculation of thermal analysis is accomplished at 30 s, which includes the cooling stage after the completion of laser cutting. In both simulations, the peak temperature of the cutting edge is controlled at 1,614 K, which is the melting temperature of the material. The simulation and the experiment showed similar results. By comparing Fig. 15a and b, the temperature of the workpiece with 2-mm thickness is slightly higher than that with 1-mm thickness.

Figure 16 shows the 3D view of the von Mises stress distribution for 1- and 2-mm-thick Inconel 718 sheet. Figure 17 shows the temporal variation in von Mises stress at different locations of the cutting edge. The highest stress level was observed at the central region of the workpiece (x=25 mm) as the material is constrained to expand at both ends. Figure 18 shows the comparison of the peak von Mises stress variation along the y-axis for the two thicknesses. The graph shows that the peak stress level at the cutting edge (y=0 mm) for the 2-mm thickness is 2.08E+09 Pa, which is slightly higher than the peak stress for the 1-mm thickness, 2.05E+09 Pa. However, the results in Table 4 clearly shows that the peak stress levels at the center (z=thickness/2) of workpiece with 2 and 1-mm thicknesses are 2.48E+09 and 2.06E+09 Pa, respectively, indicating a 21% difference. This result is due to the energy stored in the cutting edge region of the thicker workpiece, which is higher during the cutting process and thereby resulting in a higher stress level [12].

Some shallow surface cracks were found at the cutting edge as shown in Fig. 19. The causes of the cracks may be complicated. One of the causes is the rapid temperature change at the cutting edge, which causes the stress to exceed the strength of the material [12, 13, 22]. In the experiment, surface cracking was found to be more pronounced at the central region. This result may be due to the higher stress in this region as shown in Table 4 above.

5 Conclusions

Laser inert gas cutting of 1- and 2-mm-thick Inconel 718 was conducted using finite element simulation. The cutting process was simulated by applying Gaussian-distributed moving heat flux as the laser heat source and element death methodology in ANSYS to remove the molten material. The simulation results show that the kerf width increases with an increase in laser power and decreases with an increase in cutting speed, which is in good agreement with the experimental results and theory. Thermal analysis results also show that the temperature rises sharply in the region close to the laser heat source. However, the temperature gradient reduces sharply and gradually when the distance increases from the cutting edge. In addition, the high-temperature gradient in the cutting edge causes the high thermal stress in the region. The stress level is highest

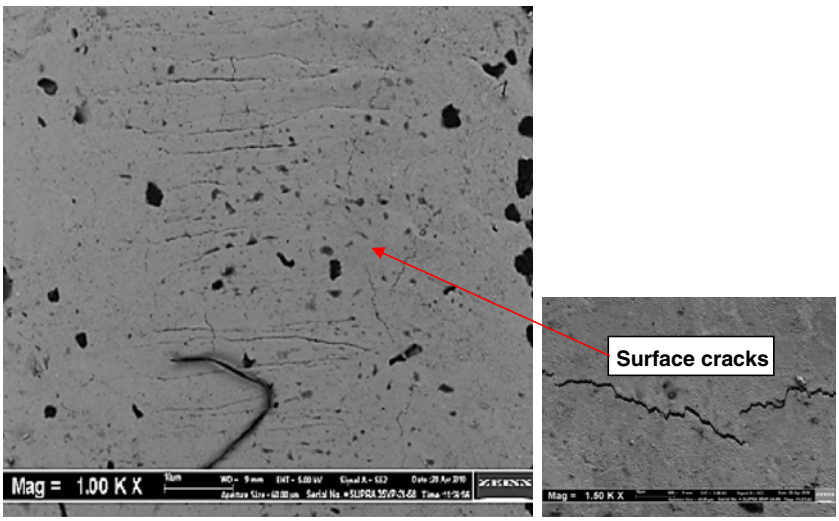

Fig. 19 SEM micrographs of the cutting edge

at the central region as the material is constrained to expand at both ends. Further, the stress level is higher for the 2-mm-thick workpiece compared with 1-mm-thick one. However, the stress levels at the surfaces, (i.e., top and bottom) of both are similar. Therefore, significant changes in thermal stress occur at the central region in the *z*-direction. A similar situation is also observed from SEM analysis as the surface cracking is more pronounced at the central region.

Acknowledgments The authors acknowledge the Universiti Sains Malaysia Science Fund project grant no. 6013362 provided by the Ministry of Science, Technology, and Innovation, Malaysia and USM-RU-PRGS project grant no. 8031011 from Universiti Sains Malaysia.

References

1. Arif AFM, Yilbas BS (2008) Thermal stress developed during laser cutting process: consideration of different materials. Int J Adv Manuf Technol 37:698–704
2. Steen WM (1991) Laser material processing. Springer, London, pp 72–80
3. Prusa JM, Venkitachalam G, Molian PA (1999) Estimation of heat conduction losses in laser cutting. Int J Mach Tools Manuf 39:431–458
4. Zhong Ji, Shichun Wu (1998) FEM simulation of the temperature field during laser forming of sheet metal. J Mater Process Technol 74:89–95
5. Ho CY, Wen MY, Ho JE, Chen DY (2007) Temperature history for cutting ceramics preheated by a CO_2 laser. J Mater Process Technol 192–193:525–531
6. Sheng PS, Joshi VS (1995) Analysis of heat-affected zone formation for laser cutting of stainless steel. J Mater Process Technol 53:879–892
7. Meung Jung Kim (2005) 3D finite element analysis of evaporative laser cutting. Appl Math Model 29:938–954
8. Akarapu R, Li BQ, Segall A (2004) A thermal stress and failure model for laser cutting and forming operations. J Fail Anal Prev 5:51–62
9. Chen M-F, Wang Y-H, Hsiao W-T (2009) Finite element analysis and verification of laser marking on eggshell. J Mater Process Technol 209:470–476
10. Sundar M, Mativenga PT, Li L, Crouse PL (2009) Laser removal of TiN from coated carbide substrate. Int J Adv Manuf Technol 45:1169–1178
11. Yilbas BS, Arif AFM (2008) Modelling of residual stresses during laser cutting of small-diameter holes. Proc Instn Mech Engrs Part B: J Eng Manuf 222(12):1577–1587
12. Yilbas BS, Arif AFM, Abdul Aleen BJ (2009) Laser cutting of large-aspect-ratio rectangular blanks in thick sheet metal: thermal stress analysis. Proc Instn Mech Engrs, Part B: J Eng Manuf 223 (1):063–071
13. Arif AFM, Yilbas BS, Abdul Aleem BJ (2008) Laser cutting of thick sheet metals: residual stress analysis. Opt Laser Technol 41:224–232
14. Yilbas BS, Arif AFM, Abdul Aleen BJ (2009) Laser cutting of holes in thick sheet metals: development of stress field. Opt Laser Technol 47:909–916
15. Yilbas BS, Arif AFM, Abdul Aleen BJ (2010) Laser cutting of sharp edge: thermal stress analysis. Opt Laser Technol 48:10–19
16. Bahotre NB, Harimkar SP (2008) Laser fabrication and machining of materials. Springer, New York, pp. 51–52, 186–187
17. Ion JC (2005) Laser processing of engineering materials. Elsevier, Oxford, pp 168–169
18. Sainte-Catherine C, Jeandin M, Kechemair D, Ricaud J-P, Sabatier L (1991) Study of dynamic absorptivity at 10.6 μm (CO_2) and 1.06 μm (Nd–YAG) wavelengths as a function of temperature. J De Physique IV C7:151–157
19. Radovanovic M (2006) Some possibilities for determining cutting data when using laser cutting. J Mech Eng 52:645–652
20. Theory reference for ANSYS, ANSYS Release 10.0, ANSYS, Inc., USA
21. Yilbas BS (2004) Laser cutting quality assessment and thermal efficiency analysis. J Mater Process Technol 155–156:2106–2115
22. Yilbas BS, Arif AFM, Abdul Aleem BJ (2010) Laser cutting of rectangular blanks in thick sheet metal: effect of cutting speed on thermal stresses. J Mater Eng Perform 19:177–184
23. Special metals [Online]. Available from http://www.specialmetals.com/documents/Inconelalloy718.pdf. Accessed 12th May 2009
24. Anderson M, Patwa R, Yung CS (2006) Laser-assisted machining of Inconel 718 with an economic analysis. Int J Mach Tools Manuf 46:1879–1891